SPECIAL ISSUE ARTICLE

Applied
Ceramic
TECHNOLOGY

Fracture of all-oxide ceramic composites: Crack path analysis by surface strain monitoring

Michaela Janowski ⓘ | **Katrin Bock** ⓘ | **Judith Moosburger-Will** ⓘ | **Dietmar Koch** ⓘ

University of Augsburg, Institute of Materials Resource Management, Augsburg, Germany

Correspondence
Michaela Janowski, University of Augsburg, Institute of Materials Resource Management, 86135 Augsburg, Germany.
Email: michaela.janowski@uni-a.de

Abstract

Crack propagation in ceramic matrix composites is very difficult to observe and to quantify. To investigate crack formation in all-oxide ceramic composites, single edge notched bending tests were performed including loading-unloading cycles and online monitoring of surface deformation using digital image correlation. The crack length was calculated by the compliance method with the crack opening displacement determined optically using digital image correlation. Obtained crack length values were found to be too small considering the sample geometry. Secondly, surface strain monitoring was used to investigate the crack growth. Analysis of cyclic force-crack opening displacement curves and the results from strain monitoring indicated no major crack growth for loads below maximum force but still a moderately decay of force after onset of cracking. Graphical analysis of the surfaces of broken samples showed crack flank lengths ranging from 3 to 6 mm. Due to highly individual crack deflection mechanisms throughout the thickness of the oxide ceramic composites, deviations between front and back of specimens are found. The results demonstrate the necessity to use individual crack length measurements of each specimen for quantitative fracture mechanical evaluation. Strain monitoring during testing was shown to be a valuable tool for online crack path investigation.

KEYWORDS
ceramic matrix composites, characterization, crack growth, fracture

1 | INTRODUCTION

Ceramic matrix composites (CMC) show a quasi-ductile failure behavior, dominated by microscopic failure processes dissipating fracture energy and preventing spontaneous, instable crack growth on the macroscopic scale. Since ceramics provide a high thermal stability and mechanical strength, CMC with their enhanced damage tolerance represent the material of choice for high temperature applications, for example, in engines.[1,2] While nonoxide CMCs provide good mechanical performance at temperatures up to 1600°C, they tend to undergo oxidation embrittlement in combustion environments. In contrast, all-oxide ceramic composites (OCMC), as the widely used

alumina-based ceramics, show improved oxidation resistance but a decrease of the mechanical properties above temperatures of 1200°C, what is predominantly caused by a degradation of fiber properties.[3,4] OCMC often are designed following the weak matrix concept (WMC) to dissipate fracture energy in failure processes in the porous matrix.[5,6] This allows stronger fiber-matrix-interfaces in OCMC compared to non-oxide CMC, reducing the need for fiber coatings and subsequently reducing processing costs.[7] To summarize, OCMC are good candidates for high temperature applications in combustion environments at reduced loads. Considering the fracture behavior of CMCs, they often show an increasing resistance against crack growth with increasing crack extension, the so-called R-curve behavior, which is related to the size of the process zone in front of the crack tip. In this zone, damage processes occur, namely the formation of micro-cracks, crack-branching, and bridging effects if the crack path crosses defined structures like grains or embedded fibers.[8–10] The R-curve behavior can be visualized, for example, by an increasing fracture energy as function of increasing crack length.[11] Laffan et al.[12] highlighted the importance of stable crack growth during the fracture mechanical testing of composites for reliable characterization of material parameters. It can be realized by suitable sample geometries, for example, notched compact tension or notched three- or four-point bending samples. A sharpened notch enables crack initiation and crack growth parallel to the notch direction. Sequences of loading and unloading, as used for compliance determination in ASTM E1820,[13] support controlled crack growth in brittle materials and allow a more detailed analysis of the loaded sample at different states of testing.

For quantitative analysis of the fracture behavior both the fracture energy and the crack area are required, that is, a method to evaluate crack growth is needed. Fett et al.[9] describes optical observation to be inaccurate for determination of the onset of crack growth and favors a calculation of the crack length by compliance evaluation. It is performed based on macroscopic deformation measurements, for example, the crosshead displacement or the crack opening displacement (COD). However, the result is expected to be subject to error. The meandering of the crack path, caused by the damage-tolerant, crack deflecting behavior of fibrous composites, leads to a complex relation of macroscopic deformation and actual crack length.

The actual study continues the activities on crack investigation. It focusses on analyzing the crack path of OCMC samples subjected to three-point bending tests by analysis of the surface strain. During loading, an online optical inspection of the loaded sample in combination with digital image correlation was used. The strain results are compared to surface crack paths investigated by microscopy

and to crack lengths obtained by the common compliance evaluation, to evaluate the reliability of the different methods.

2 | EXPERIMENTAL PROCEDURES

The OCMC samples were fabricated from an all-oxide alumina-based sheet (Keramikblech type FW12, Walter E. C. Pritzkow Spezialkeramik, Filderstadt, Germany) with a thickness of $B = 2.8\ mm$. The sheet contains 1500 denier Nextel 610 fibers in a 0°/90° plain weave in an alumina-based matrix. The Keramikblech sheet was cut into single-edge-notched bend (SENB) samples using a water-cooled abrasive cut-off machine (Brillant 250, QATM, Mammelzen, Germany). The dimensions were set in accordance with geometry requirements of ASTM E1820. The geometry relations are summarized in Figure 1. Based on the thickness $B = 2.8\ mm$ of the sheet as limiting parameter, the width must be $W = 2B = 5.6\ mm$. The length L of the samples was chosen to 40 mm. For bending tests, the support length S is the defining parameter. L must amount to at least $L/2 = 2.25\ W$, resulting in a minimum length of 25.6 mm for the sample. The SENB samples were notched using a high-precision diamond wire saw (WS25, IBS GmbH, Grafrath, Germany) resulting in an average notch width of 230 μm, which is far below the maximum allowed value of 3.5 mm. Still the width is higher than 56 μm (.01 W), so sharpening of the notch tip is necessary to define the position of crack initiation and to support a largely straight and unbranched crack path. This requires a notch tip angle of ideally less than 30°. Because sharpening by fatigue cracking, as required in ASTM E1820, is not feasible with the given OCMC material, it was done using a razor blade and progressively finer diamond emulsions. This led to notch angles in the range of 20 °. The notch length a_i including the sharpened tip was in the required range of 2.8 mm, which corresponds to .5 W.

Three-point bending tests were performed using a testing machine with a 5 kN load cell (zwickiLine Z5.0 TN, Zwick & Roell, Ulm, Germany). The samples were cyclically loaded at a displacement-controlled rate of .2 mm/s. Each loading sequence was followed by an unloading sequence in which the sample was unloaded to 5 N at a rate of .4 mm/s. Up to a total displacement of 200 μm the unloading sequences were started after every 10 μm of crosshead-displacement, at higher displacements after every 50 μm. The test was stopped at a total displacement of 1 mm. During the fracture mechanical test, the crack opening displacement and the strain of the sample were measured optically using a camera system with an estimated resolution of 5 μm in the setup (Aramis 12 M,

FIGURE 1 Single-edge-notched bend (SENB) specimen geometry and testing setup with orientation of fibers depicted.
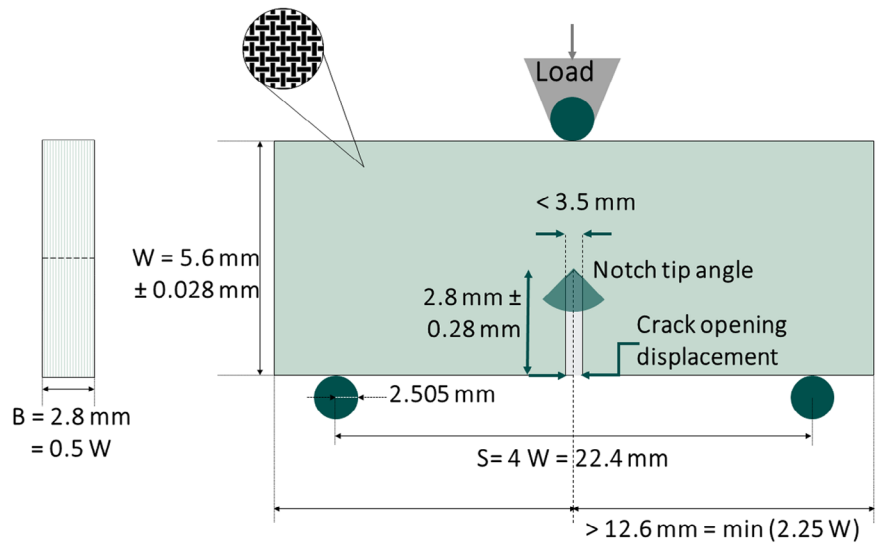
GOM, Braunschweig, Germany). One side of the sample was sprayed with a speckle pattern, which was tracked by the camera system. Through digital image correlation, distances, their respective changes, and the resulting strain values were calculated by the software associated with the camera system. These strain measurements were used for tracking the crack growth and estimating the crack length. The crack opening displacement v_i was measured by digital image correlation as the change in the distance between the notch flanks at the starting point of the notch (see Figure 1). The corresponding length was defined as a parameter in digital image correlation and calculated online during test. The crack length was also determined using the compliance C_i, which was calculated after each loading-unloading cycle by subtracting the minimum load after unloading from the maximum load before unloading. The compliance is defined by $C_i = \Delta v_i / \Delta P_i$, where ΔP_i is the load difference at cycle i and $\Delta v_i = v_{i,\,max} - v_{i,\,min}$ represents the difference in measured crack opening displacement at maximum and minimum load of cycle i. The increased crack length a_i of each cycle was calculated from geometry relations, the Young's Modulus E, and the compliance C_i, as described in ASTM E1820:

$$\frac{a_i}{W} = \left[0,999748 - 3,9504\,u + 2,9821\,u^2 - 3,21408\,u^3 \right.$$
$$\left. + 51,5156\,u^4 - 113,031\,u^5 \right] \quad (1)$$

$$u = \frac{1}{\left[\frac{BWEC_i}{\frac{S}{4}} \right]^{1/2} + 1} \qquad C_i = \frac{\Delta v_i}{\Delta P_i}$$

For the starting crack length a_0 the notch length was chosen. After fracture mechanical testing, the surfaces of
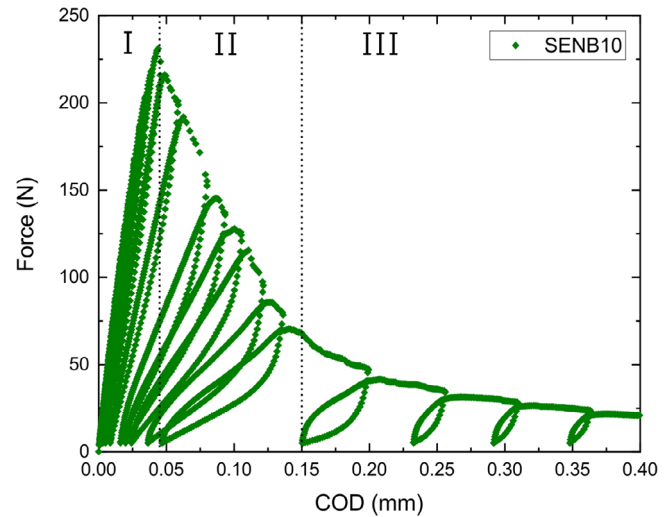
FIGURE 2 Exemplary force-crack opening displacement (COD)-curve taken during cyclic loading of specimen SENB10 with marked regions I, II, and III of changing material behavior.

sample front- and backside were examined with a digital optical microscope (VHX 6000, Keyence, Osaka, Japan). To obtain the individual crack length of the tested sample, the crack flanks of both specimen sides were measured using ImageJ (Fiji).[14]

3 | RESULTS AND DISCUSSION

The crack growth during fracture mechanical testing of OCMC SENB samples was investigated. For the SENB-tests conducted with loading-unloading cycles, maximum forces F_{max} in the range of 200–230 N were reached at COD-values around .05 mm. In Figure 2 one exemplary cyclic load-COD curve is shown. At beginning, the load
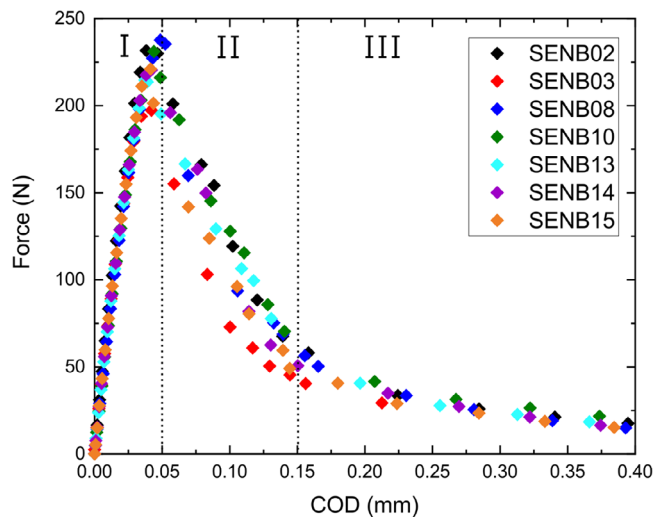
FIGURE 3 Force-crack opening displacement (COD)-curves of all tested specimens with data reduced to maximum load per cycle. Regions of changing behavior I, II, and III are marked roughly for all specimens.

increases nearly linearly with very small increases of COD per cycle. This region I, which is also marked in Figure 2, is dominated by elastic behavior. After reaching F_{max}, the COD per cycle rises simultaneously with the area enclosed in the load-displacement loops, while the maximum load per cycle decreases (region II). In region III, beginning at CODs around .15 mm, force-COD-cycles change their form significantly. The loading-unloading cycles become much broader while the forces at the end of loading are small, indicating a strongly damaged sample. Contributing to the damage tolerant failure behavior of OCMCs, a certain strength remains for the samples, preventing catastrophic failure. Region III is neglected in further analysis of the crack paths.

In Figure 3 the results of seven tested specimens are summarized. For improved readability, data were reduced to the forces and corresponding COD values at the end of each loading cycle. In region I clearly linear behavior is observed. Depending on the individual specimen, only small deviations from linearity can be seen before reaching the respective F_{max}. Also scattering of the forces is small in region I. Scattering increases rapidly in region II after reaching F_{max}, when load drops with each cycle until reaching the damaged state of region III. These observations prove similar elastic behavior and strength of all samples, but highly individual crack growth due to statistically different deflection at fibers and pores in the matrix.

From the differences between loaded and unloaded state of each cycle, the compliance in dependence of COD was calculated for each specimen (see Figure 4A). In region I the compliance values increase linearly but on a small

scale while they increase rapidly in region II after reaching the COD at F_{max} (see cutout in Figure 4B). Although values scatter among individual specimens in region II, their behavior still is similar. In region III the compliance collapses to negative values caused by a rapidly increasing COD beyond .15 mm, resulting in negative values of Δv_i. With this significant change in behavior, clearly visible in Figure 2, the specimens are defined as destroyed at this point.

The compliance values indicate no onset of major crack growth before reaching the COD corresponding to F_{max} at the end of region I. In most cases, the first significant difference was found for the first or second cycle after reaching F_{max}. The slight increase of compliance at CODs below .05 mm is attributed to energy dissipation by microcracking within the matrix, which does not cause a decrease of applicable stress at this state of loading. However, microcracking cannot be determined in detail by the used methods of observation, even though it is indicated by a considerable large zone of surface strain perpendicular to the notch direction, as described below.

Since according to ASTM E1820 compliance and crack length correlate, a rapid increase of the crack length can be stated, as illustrated in Figure 5 for all specimens. The crack lengths calculated for each cycle show similar behavior but with the same restrictions at state of heavily damaged samples in region III. This is demonstrated, e.g, by specimen SENB3 (red in Figure 5) at CODs between .14 and .16 mm. In this case, calculation failed to provide accurate crack growth rates resulting in seemingly decreasing values of crack length at increasing deformation of sample.

The final crack length was obtained by calculation following equation (1) and subtracting the notch length, which was used as starting length a_0. The average final crack length for all specimens at the end of testing was found to be 1.58 ± .33 mm. Taking into account the sample height of $W = 5.6\ mm$ and the average notch length of 2.73 ± .05 mm, the crack would not reach throughout the sample. Since in addition the meandering of the crack path further increases the absolute crack length, the values obtained by the compliance calculation are far too small. This was affirmed by analysis of optical micrographs of the specimen surfaces with respect to the crack path. The crack flanks visible on both sides of the specimen were identified and their corresponding lengths were measured by ImageJ. Exemplary for specimen SENB10, the identified crack flanks on front- and backside are shown in Figure 6. It should be noted that the frontside is covered by the speckle pattern, while the backside is in its original state. The resulting average crack lengths (not including notch length) were measured to 3.48 ± .28 mm for the
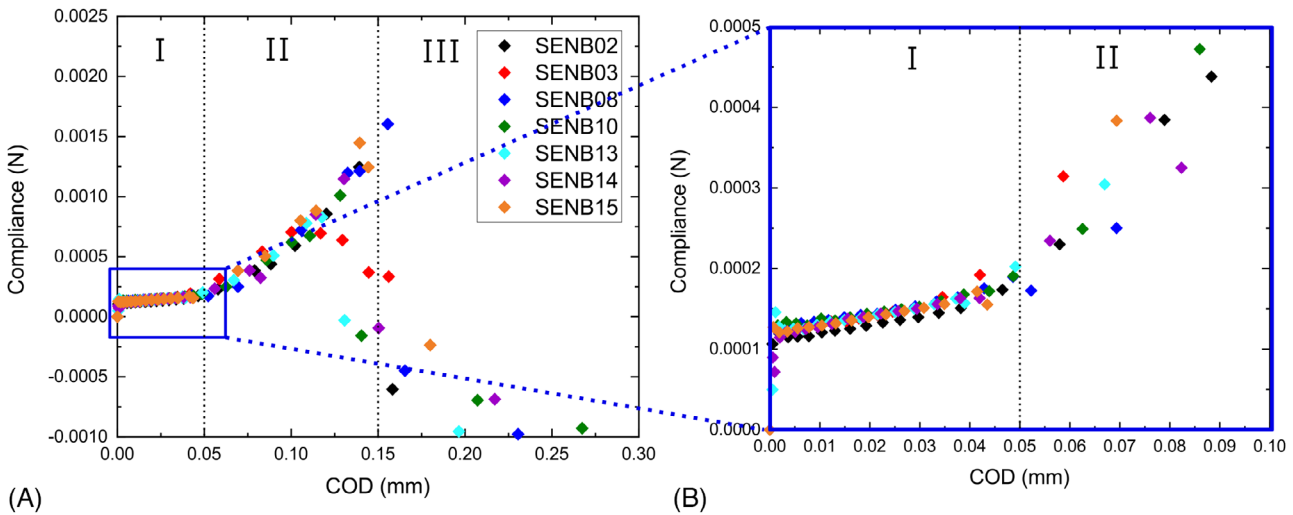
FIGURE 4 (A) Compliance-crack opening displacement (COD)-curves and (B) closer inspection for small COD-values. Regions I to III are marked roughly for all specimens.
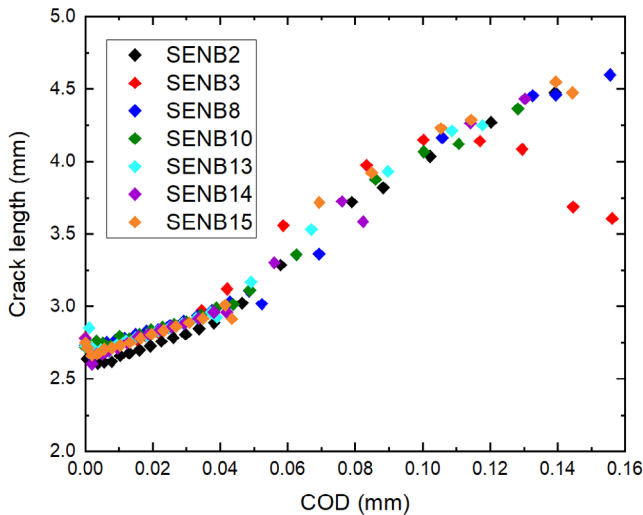

FIGURE 5 Increase of crack length (including the notch length) calculated by compliance method according to ASTM E1820 in dependence of crack opening displacement (COD).

front- and $5.38 \pm .27$ mm for the backside, respectively. Redrawing the flanks as vector objects allows a graphical overlapping for closer analysis (see Figure 7). Inaccurate matching of the two corresponding crack flanks on one surface (Figure 7A,B) indicates a certain degree of delamination at the surface layers in vicinity of the crack flanks, leading to smaller particles chipping off. Corresponding crack paths of front- and backside of a specimen show even stronger deviations (see Figure 7C)), with the crack on the frontside showing a less curved course. For the majority of the samples, the paths on the frontside are shorter than on the backside, leading to averaged crack lengths of $4.13 \pm .78$ mm for front- and of $5.03 \pm .85$ mm for backside, respectively. The different appearance of the crack

on sample front- and backside partly is due to the different meandering of the crack within the sample material. In addition, the definition of the crack flanks probably is influenced by the speckle pattern applied to the frontside. Though it simplifies optical detection of the crack, it is also assumed to cover details of the fracture process. The observed differences on front- and backside demonstrate the problem of surface analysis for crack path determination, which is not able to follow the crack growth within the sample volume.

During cyclic testing, local surface strain was online monitored optically and was visualized by a colormap, defined by blue areas for compressive strain changing to red for tensile strain with a scale ranging from $-.5\%$ to $+.5\%$ (see for specimen SENB10 in Figure 8). During loading, non-contiguous, elastically .5%-strained areas located perpendicular to the designated crack path spread over the surface close to the notch tip. This is shown in Figure 8A,C for the maximum loaded state of the respective cycles. The effect occurs to be elastic, as in unloaded state it is no longer detectable (see Figure 8B,D). Before reaching maximum force F_{max} of the specimen, this perpendicular spreading of strain seems to be the predominant deformation. Strain of .5 % at the notch tip following the notch direction occurs first as elastic deformation. A portion of the main crack related strain is visible right at the notch tip parallel to notch direction in Figure 8A. It vanishes in the unloaded state of Figure 8B but is visible again in Figure 8C at loaded state as part of the strained area. The strain becomes persistent in the following unloaded state as shown in 8D, indicating the beginning of critical crack growth. This is similar for all specimens, though the onset of persistent strain varies between the first and third cycle after reaching F_{max}. With ongoing deformation, the per-
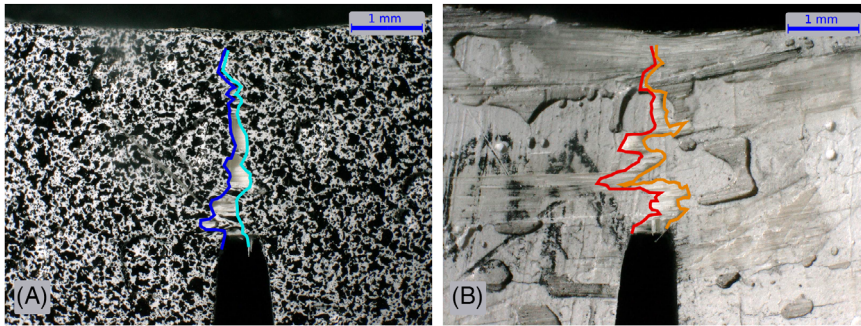
FIGURE 6 Graphical crack path analysis (A) of specimen SENB10's painted frontside and (B) of original backside.
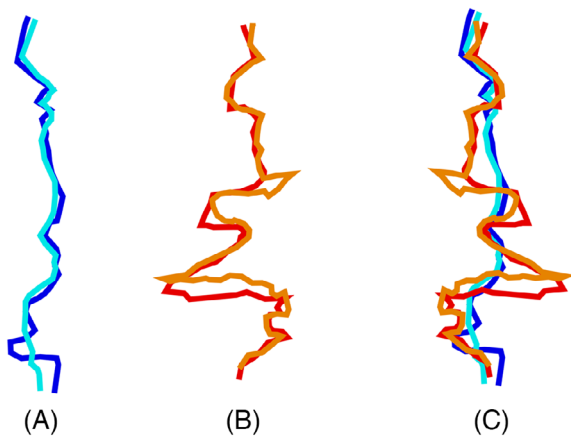

FIGURE 7 (A) Crack paths of frontside; (B) crack paths of backside; (C) overlapping of paths of front and back side.

sistently strained area increases following the designated path direction. With end of loading region II (see Figure 2), large deformation occurs in front of the notch tip causing the strain calculation to fail (see Figure 9). This is the onset of visible crack opening. The specimen is considered to be heavily damaged at this point. Comparing the visible crack at the end of the test with the calculated surface strain, the latter covers a larger area than the crack and is located next to and parallel to the crack flanks. Only one single crack without branching was formed in specimen SENB10, as introduced by the sharpened notch. For the other specimens, branching was also not detectable, though it could be suggested for visible defects of some specimens. But these observations, always limited to only one side of the respective specimen, were caused by delamination of surface layers and consequent chipping off of these areas. No precise information about microcracking can be obtained by these experiments. However, the strained areas surrounding the visible crack indicate a considerable large process area perpendicular to the notch direction. Comparing their size with that of persistent areas after critical load (see Figure 8D), formation of microcracks already in loading zone II must have occurred. Since also relaxation occurs, only the main crack remains visible in the strain map.

4 | SUMMARY AND CONCLUSION

Single edge notched bending test was performed on all-oxide ceramic samples using loading-unloading sequences. The samples showed similar elastic properties at the beginning of testing. With increasing load, crack growth following notch direction without branching was observed. This facilitates the measurement of crack length and an analysis of crack path formation. Using the optically determined crack opening displacement and the force measured during testing, the compliance was calculated according to ASTM E1820. This led to crack lengths around 1.58 mm, being too small with regard to the specimen geometry and observations. This result was confirmed by analysis of the crack paths using optical microscopy. Comparing all tested specimens, highly individual crack growth after initiation of the main crack was observed. The meandering of the crack path was clearly detectable by optical microscopy, further increasing the final crack length to values between 3 and 6 mm. However, the visible crack paths deviate between front- and backsides of the specimens because of the different deflection within the volume. This shows the complexity in determining a crack area for quantitative fracture energy calculation. The crack paths of the sample frontsides are in good agreement with the surface strain measured optically during testing. Online strain measurements further indicate initiation of crack growth shortly after reaching maximum force. This was affirmed by analysis of force-displacement curves as well as compliance calculation. Though microcracking could not be determined with these experiments, it was indicated by the strain monitoring. Concluding, the SENB test setup leads to unbranched cracks following the orientation designated by the prepared notch in all-oxide ceramic composites, but crack path formation remains individually to the respective specimen. Surface strain monitoring was shown valuable for investigation of the crack path, in particular in the early stages of loading, where the crack is not detectable by usual optical methods. The results showed the possibility of determining the crack length by optical measurements. Future investigations
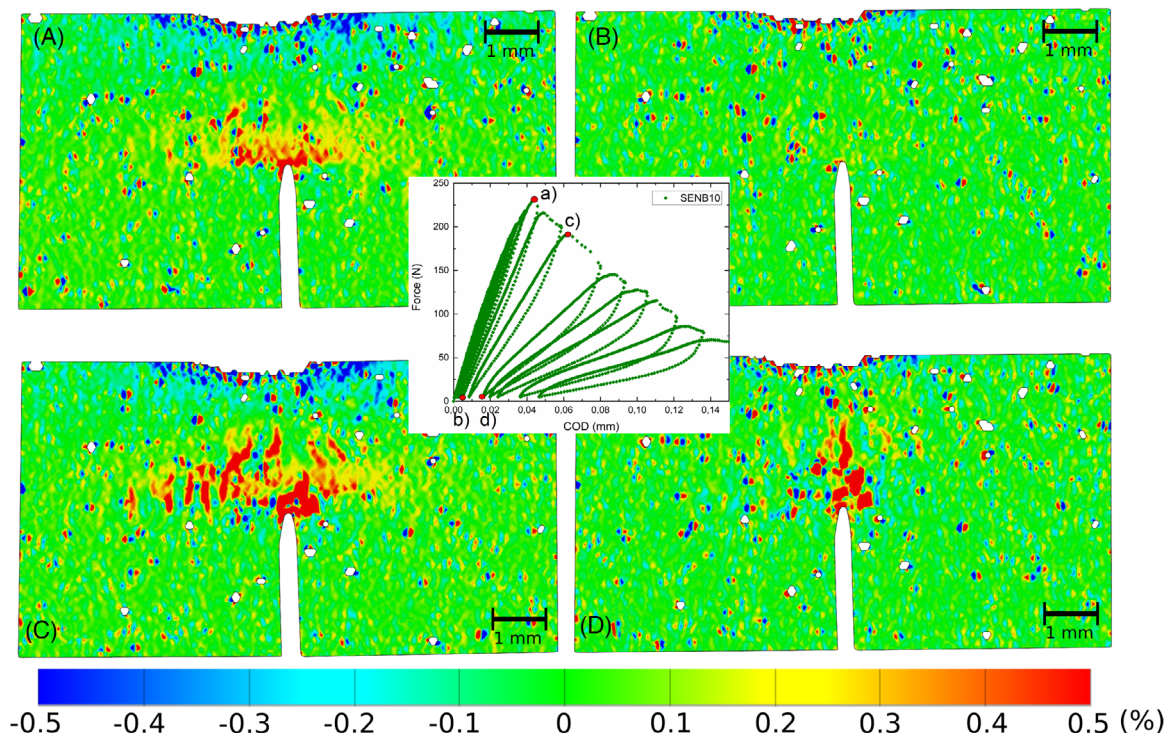
FIGURE 8 Surface strain of specimen SENB10 during loading visualized by colormap reaching from −.5% to +.5% strain (A) in loaded state at F_{max}; (B) in unloaded state directly after reaching F_{max}; (C) in loaded state at second cycle after reaching F_{max}; (D) in unloaded state at second cycle after reaching F_{max}.
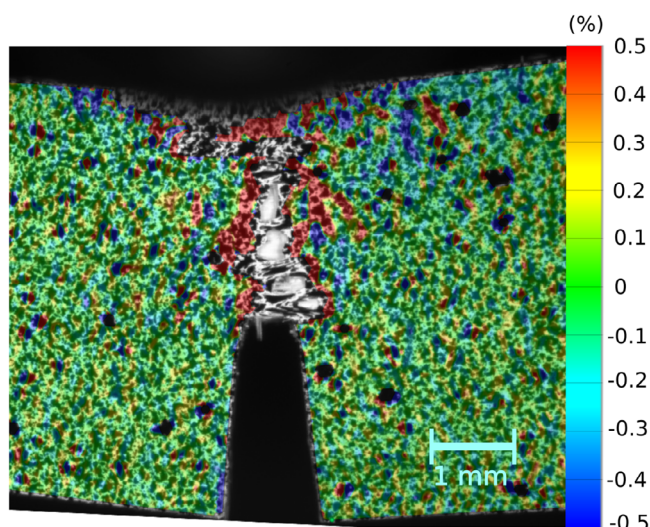
FIGURE 9 Visibly opened crack and end of test of specimen SENB10 with corresponding surface strain monitoring.

shall lead to a correction factor, considering the average crack path deviations of individual planes within the volume of a specimen, to estimate a reliable total fracture area of a sample. The fracture toughness then will be calculated only monitoring one single surface of a sample during testing. This will save time and effort in characterizing all-oxide ceramic composites for technical applications.

ORCID

Michaela Janowski https://orcid.org/0000-0002-6783-0477
Katrin Bock https://orcid.org/0009-0000-6534-1920
Judith Moosburger-Will https://orcid.org/0000-0001-9137-980X
Dietmar Koch https://orcid.org/0000-0003-4504-8721

REFERENCES

1. Schlacher J, Jabr A, Hofer A-K, Bermejo R. Contact damage tolerance of alumina-based layered ceramics with tailored microstructures. J Am Ceram Soc. 2022;105:4387–99.
2. Ramachandran K, Leelavinodhan S, Antao C, Copti A, Mauricio C, Jyothi YL, et al. Analysis of failure mechanisms of oxide—oxide ceramic matrix composites. J Eur Ceram Soc. 2022;42:1626–34.
3. Karadimas G, Salonitis K. Ceramic matrix composites for aero engine applications—a review. Appl Sci. 2023;13:3017.
4. Zok FW. Developments in oxide fiber composites. J Am Ceram Soc. 2006;89:3309–24.
5. Zok FW, Levi CG. Mechanical properties of porous-matrix ceramic composites. Adv Eng Mater. 2001;3:15–23.

6. Kupsch A, Laquai R, Müller BR, Paciomik S, Horvath J, Tushtev K, et al. Evolution of damage in all-oxide ceramic matrix composite after cyclic loading. Adv Eng Mater. 2022;24: 2100763.

7. Pritzkow WEC, Almeida RSM, Mateus LB, Tushtev K, Rezwan K. All-oxide ceramic matrix composites (OCMC) based on low cost 3 M Nextel™ 610 fabrics. J Eur Ceram. 2021;41:3177–87.

8. Munz D. What can we learn from R-curve measurements? J Am Ceram Soc. 2007;90:1–15.

9. Fett T, Fünfschilling S, Hoffmann MJ, Oberacker R, Jelitto H, Schneider GA. R-curve determination for the initial stage of crack extension in Si 3 N 4. J Am Ceram Soc. 2008;91:3638–42.

10. Laffan MJ, Pinho ST, Robinson P, McMillan AJ. Translaminar fracture toughness: the critical notch tip radius of 0° plies in CFRP. Compos Sci Technol. 2011;72:97–102.

11. Krüger L, Trubitz P. Henschel S. [Fracture mechanics at static and dynamic loading]. In: Biermann H, Krüger L, editors. [Modern methods of testing materials]. Weinheim, Germany: Wiley-VCH; 2015. p. 1–52. German.

12. Laffan MJ, Pinho ST, Robinson P, McMillan AJ. Translaminar fracture toughness testing of composites: a review. Polym Test. 2012;31:481–89.

13. American Society for Testing and Materials E 1820-20b. Standard test method for measurement of fracture toughness. ASTM International in West Conshohocken, PA; 2020. https://doi.org/10.1520/E1820-20B

14. Schindelin J, Arganda-Carreras I, Frise E, Kaynig V, Longair M, Pietzsch T, et al. Fiji: an open-source platform for biological-image analysis. Nat Methods. 2012;9:676–82.